Preliminary results from the New Deformation multi-anvil press at the Photon Factory: insight into the creep strength of calcium silicate perovskite.

Andrew R Thomson[1], Y. Nishihara[2], D. Yamazaki[3], N. Tsujino[3], Simon A Hunt[4], Y. Tsubokawa[5], K. Matsukage[6], T. Yoshino[3], T. Kubo[5], David P Dobson[1]

[1]Department of Earth Sciences, University College London, London, WC1E 6BT, United Kingdom
[2]Geodynamics Research Center, Ehime University, Matsuyama, 790-8577, Japan
[3]Institute for+ Planetary Materials, Okayama University, Misasa, 682-0193, Japan
[4]Department of Materials, University of Manchester, Manchester, M1 3BB, United Kingdom
[5]Department of Earth and Planetary Sciences, Kyushu University, Nishi-ku, 819-0395, Japan
[6]Department of Natural and Environmental Science, Teikyo University of Science, Yamanashi, 409-0193, Japan

Abstract.

A D111 deformation multi-anvil press, which is a larger version of the Deformation T-cup, has been installed at beamline NE7A at PF-AR, KEK, Tsukuba, Japan. Using this apparatus, controlled deformation experiments can be performed by independently moving two opposite second-stage anvils in a Kawai-type 6/8 geometry. This allows both pure and simple shear experiments with sample strain rates of ~ 10^{-6} s^{-1} to be conducted at pressure and temperature conditions up to at least 27 GPa and 1700 K. Here the capabilities of the D111 press are demonstrated using experiments investigating the creep strength of calcium silicate perovskite at mantle conditions. Experiments performed at ~ 13 GPa and 1150-1373K with quantitative stress and strain rate measurements have allowed preliminary evaluation of the creep strength of calcium silicate perovskite. Observations indicate that under dry and wet conditions samples possess grainsizes of between 0.5 and ~ 10 μm, and undergo deformation in a diffusion creep regime with an apparent activation energy of ~ 364 kJ mol^{-1} and a stress exponent of 1.28. Qualitative comparison of preliminary results with the properties of mantle silicate minerals including bridgmanite, wadsleyite and dry olivine indicates that calcium silicate perovskite is very weak, such that it may strongly influence the geodynamics of the deep mantle especially in regions of subduction.

Introduction.

Compared to the other rocky planets, Earth is dynamic, with an active dynamo, volcanism, seismicity and repeated, continuous, cycling of material between the surface and deep interior for at least the last 2.5 billion years (Krusky et al., 2001). The plate-tectonic style of convection appears to be unique to the Earth and results in regions of dynamic complexity at the surface and the core-mantle boundary, the major thermal boundary layers of the mantle system. Geophysical studies show a third region of complexity in the mid-mantle, associated with the stabilisation of silicate perovskite around 660 km depth. In this region, subducted slab material shows a wide range of complex behaviours, ranging from penetration into the lower mantle, through ponding around 1000-1200 km depth, to stagnation in the transition zone (van der Hilst, 1995). This tomographically-imaged complexity is accompanied by further evidence of basalt enrichment in the region around 660 km (Greaux et al. 2019; Thomson et al., 2019*),* implying that subducted crustal mid-ocean-ridge-basalt (MORB) can mechanically decouple from the depleted, ultramafic components of the slab interior. The complex behaviour of the subducting slab is likely to be due to changes in density and, more importantly, viscosity of the slab and surrounding mantle as the Mg_2SiO_4-dominated upper mantle mineral assemblages transform into $MgSiO_3$-bridgmanite dominated assemblages in the lower mantle (e.g. Karato, 1997). The rheological behaviour of the crustal components of subducting slabs are further complicated in this region because of its more silica- and calcium-enriched chemistry compared with ultramafic lithologies, which results in a distinct bulk mineralogy in the transition zone and lower mantle variously containing components of stishovite, $CaSiO_3$ perovskite, NAL phase and CF-phase (e.g. Perrillat et al., 2006).

In order to understand this complexity and to accurately model the convective behaviour of the mantle it is necessary to measure the thermoelastic and rheological properties of the constituent rocks and minerals under the appropriate conditions of pressure, temperature and stress. There has therefore been considerable effort to develop apparatus to maintain simultaneous high pressure and temperature in macroscopic (~mm^3) samples for extended durations and, recently, to modify these presses to allow controlled deformation of samples under mantle conditions. The most successful static large-volume high-pressure devices are multi-anvil presses where steel wedges transfer load from the press ram(s) to an inner arrangement of anvils composed of tungsten carbide or other, super-hard, materials (Kawai and Endo, 1970; Kawai et al., 1973; Shimomura et al., 1985; Ito et al., 2007; for a review of multi-anvil history see Liebermann, 2011). These inner anvils compress a ceramic pressure cell which itself contains an electrically conductive furnace, insulation materials, means of measuring temperature, and sample capsule. There is a very large stress gradient between the high-pressure region within the ceramic cell, which can be at several tens of gigapascals, and the air gap between the inner anvils and much effort has been invested in optimising the materials of the cell and gaskets, and the geometry of the press. Currently the highest pressures are attainable using an arrangement where an octahedral pressure cell is compressed by 8 hard inner (second-stage) anvils which pack together to form a cubic volume (figure 1 A, B). This cubic 'nest' is compressed by 6 (first-stage) steel wedges (the 6/8 multi-anvil arrangement) with either a 3-fold (111) or a 4-fold (100) axis aligned parallel to the direction of compression of the primary press ram. The last two decades have seen the development of deformation multi-anvil presses where one opposing pair of anvils can be advanced (or retracted) independently of the remaining anvils, applying an approximately axi-symmetric strain to the pressure medium and sample. The d-DIA geometry (Fig. 1C) applies strain along the 4-fold axis of a cubic carbide anvil set in a single stage press (Wang et al., 2003) and has been combined with synchrotron radiation at several facilities (e.g. Nishiyama et al., 2008, Guignard and Crichton, 2015, Wang et al., 2019, Farmer et al., 2020). The single stage (6-anvil) DIA geometry is limited to about 10 GPa confining pressure, which can be increased in the 6-6 geometry using multi-staging coupled with anvil guides to reach ~ 18 GPa (Nishiyama et al., 2008; Kawazoe et al., 2016). Alternatively, the d-DIA can be used with an internal 6-8 geometry cube-set to performed deformation experiments at conditions reaching ~ 25 GPa (Fig. 1D) (Tsujino et al., 2016). However, in the 6-8 implementation of d-DIA the deformation axis is co-axial to the (100) axis of the octahedral pressure cell (and hence centred on the gaskets, rather than through an anvil). This results in complex sample strain possibilities due to gasket relaxations along the compression axis. An alternative deformation press geometry (Fig. 1E, F), the deformation-T-cup, was developed over the last decade (Hunt et al., 2014, 2019; Hunt and Dobson, 2017). This is based on the Kawai-type 6/8 geometry and the deformation axis is oriented along the (111) axis, centred on a pair of opposed anvil faces. This geometry is capable of controlled deformation at sample pressures in excess of 23 GPa and, here, we report the implementation of this deformation geometry at beamline NE7A of the Photon Factory at KEK and demonstrate its capabilities using preliminary data collected on $CaSiO_3$ perovskite samples.

The D111 Press on NE7A at KEK.

The deformation geometry employed in the D111 press is described elsewhere (Hunt et al., 2014) so here we will concentrate on details specific to this implementation. A cutaway schematic of the press tooling installed on beamline NE7A is shown in Figure 2A. The tooling is designed to be a compact single unit which can be replaced in the press with alternative tooling geometries. Oil-driven secondary actuators which control the uniaxial deformation of the cell are contained within the guide blocks of the tooling so the primary pressure generation is driven using a standard single-piston four-post press. This means that, if the secondary actuators are not moved during an experiment the system behaves identically to a traditional Kawai-type hydrostatic multi-anvil press. The implementation on beamline NE7A uses the existing 700 ton MAX-III press and is interchangeable for different tooling designs. In the Kawai geometry, each second-stage anvil experiences loads of up to 175 tons from the main ram. The differential actuators have a capacity of 314 tons each but only act on a single anvil – this excess load capacity in the differential actuators ensures that frictional losses can be overcome, and deformation is possible right up to the 700 ton maximum load of the press. The two deformation anvils are advanced by pumping oil into the secondary actuators. This shortens the octahedral pressure medium along its vertical (111) symmetry axis and the anvils in the equatorial plane dilate in response to the reduced component of the main-ram end load which they are supporting.

High-pressure cells and carbide tooling are constructed and loaded in the standard manner for 6/8 experiments, with the addition of hard components along the cell axis to transfer differential stress to the sample. This cubic nest of second-stage anvils and cell are loaded into the D111 tooling outside the press frame (Fig. 2B) with a (111) symmetry axis vertical. The first-stage Kawai-geometry wedges compress 6 of the 8 second-stage anvils but the two anvils which align along the vertical (111) axis (labelled (3) in Fig. 2A) are compressed by a hexagonal arrangement of pistons which communicate to the deformation actuators. The original hexagonal deformation pistons of Hunt et al. (2014) are split such that the hexagonal column which supports the deformation anvils is composed of three identical pieces, each occupying 120 degrees of rotation about the (111) symmetry axis (Hunt and Dobson, 2017). The front ends of these pieces are ground such that when installed they support the entire back faces of the second-stage carbide deformation anvils. This improves anvil performance over the original D-T-cup design (Hunt and Dobson, 2017). Similarly, to the deformation-DIA geometry the primary mode of deformation in the D111 geometry is axi-symmetric, resulting in a pure shear sample deformation mode. The axi-symmetric cell deformation can be transformed into simple shear deformation by placing the sample between pistons whose ends are cut at 45 degrees (Karato and Rubie, 1997).

In the D111 implementation at beamline NE7A X-rays traverse the second-stage anvil set perpendicular to the vertical mirror plane of the second-stage anvils and octahedral pressure cell (Fig. 1F) passing through two diagonally opposite gaskets. The pyrophyllite gaskets through which X-rays pass are replaced by a low-absorbing, typically B-dominated, gasket material. Careful alignment of the first stage anvil wedges within the split confining ring is required to ensure that the X-ray cut-outs maintain the correct geometry with respect to the X-ray beam (Fig. 2B), which can also be adjusted by rotating the entire MAX-III load frame. The beamline delivers a photon flux of 10^8-10^9 $mm^{-2}s^{-1}$ over a 3 mm high by 80 mm wide beam, measured at 20 m from the source. The photon energy range is 10-140 keV and the beamline can be operated in white beam or monochromatic (10-60 keV) modes. In order to perform successful rheological experiments either X-ray transparent anvils (e.g. PCD or cBN) or carbide anvils with suitable slot/cone cut-outs are used in place of the downstream second stage anvils to allow sufficient radiographic and diffraction data collection (Dobson et al., 2012; Irifune et al., 1992).

Stress-strain data on NE7A are collected by combined radiography and diffraction using a monochromatic incident X-ray beam and angle-dispersive diffraction. This is generated by passing the raw synchrotron beam through a two-crystal Si(111) monochromator to achieve an incident beam with monochromatic energy of 50-60 keV. The transmitted X-ray beam is typically imaged using a YAG(Ce) or GAGG(Ce) scintillator crystal combined with a CCD or CMOS camera positioned downstream of the sample on motorized linear translation stages. Highly absorbent foils (typically Au, Pt or Re) are placed on both ends of samples as strain markers which show up in the radiographic images, allowing changes in the sample length (and strain rate) to be monitored throughout deformation experiments. Radiographic images are normally 0.5 – 5 s in duration, depending on the absorption properties of the sample assembly. Their resolution depends on the exact camera model used, however is typically around 1 μm which is sufficient to allow strains of 10^{-3} to be monitored in millimetre sized samples when an appropriate cross-corelation algorithm is employed (e.g. Li et al., 2003). Diffraction patterns are collected using a Dexela 2923 area detector, whose position is calibrated using a certified standard material (CeO_2 in this study). Individual diffraction patterns are collected from an illuminated sample area defined using collimation slits placed upstream of the sample position and typically have durations of 1-4 minutes depending on sample characteristics. During experiments the lattice strain of each sample is determined from the azimuthal distortions of the Debye-Scherrer rings from the polycrystalline samples. Lattice strain is subsequently converted into a stress measurement by utilising the elastic moduli of the sample material, which are required to be known prior to experiments. This experimental approach has been widely applied in d-DIA and 6/8 geometries at global synchrotron sources and achieves stress resolution, depending on the elastic properties of the sample, of ~ 100 MPa for most silicate minerals. Each data collection cycle consists of sequential X-ray radiographic images followed by X-ray diffraction pattern collections, between which both the diffraction slits and CCD/CMOS imaging camera are moved into/out of the X-ray beam path using motorized linear translation stages. The total time for each data collection cycle can vary between approximately 2 and 8 minutes depending on the required radiograph and diffraction times, and whether one or two samples are being monitored throughout deformation. A schematic of the experimental setup of the D111 on NE7A is provided in figure 3.

The D111 setup on NE7A has so far been used to perform deformation experiments using various sized multi-anvil assemblies at primary ram loads up to ~ 500 tonf coupled with 2, 3 or 5 mm truncations. Samples investigated to date have included hcp iron, bridgmanite, ringwoodite and $CaSiO_3$ perovskite (Ca-Pv) which have been studied at a range of pressure and temperature (*PT*) conditions extending between 12 – 27 GPa and 650 – 1700 K with strain rates of $1 \times 10^{-6} – 1.1 \times 10^{-4}$ s^{-1} (figure 4, after Nishihara et al., 2020). In the subsequent sections of this paper we describe initial experiments performed to investigate the rheological properties of Ca-Pv. These provide a demonstration of the current capabilities and examples of data that can achieved using the existing D111 system on NE7A.

The rheological behaviour of Ca-Pv

Ca-Pv is one of the major mineralogical constituents of Earth's deep mantle and is thermodynamically stable at pressures from ~ 10 GPa to the core-mantle boundary. After entering the phase assemblages of subducting lithologies at ~ 19-21 GPa (Holland et al., 2013) it constitutes ~5 to ~30 wt.% of depleted ultramafic to mafic lower mantle assemblages respectively (e.g. Kesson et al., 1998; Perrillat et al., 2006). At these abundances, especially in subducting mafic assemblages, Ca-Pv is sufficiently abundant that it might well form an interconnected network of grains (Handy et al., 1994). In this situation, depending on the rheological properties of Ca-Pv, it may dominate the strength of subducting mafic lithologies and potentially be important in controlling on the geodynamics of subduction and slab delamination throughout the transition zone and lower mantle.

Studies of Ca-Pv are complicated by the inability to recover samples of it from synthesis to ambient conditions, as it spontaneously undergoes amorphization during decompression at room temperature (e.g. Liu and Ringwood, 1975, Wang et al., 1994). This feature of Ca-Pv means that many of its physical properties, including its elastic and rheological properties, are poorly understood and can only reasonably be assessed using *in-situ* experiments where it can be synthesised and investigated in a single experimental run. Synchrotron-based large volume press experiments (e.g. Wang et al., 1994, Greaux et al., 2019, Thomson et al., 2019) provide a suitable approach which can achieve this, and here we present our initial experimental results to constrain the viscous strength of Ca-Pv at *PT* conditions inside its stability field using the KEK D111 press.

Experimental details.

As the elastic moduli of Ca-Pv, which are required for experimental stress measurements, are poorly known two experimental setups were used in this study. Whilst a solitary sample of Ca-Pv was studied in one experiment, 2 further experiments utilised a deformation column containing stacked samples of olivine and Ca-Pv. Starting materials for all deformation experiments consisted of sintered cylinders of synthetic olivine and wollastonite. Cylinders of fine-grained powder, ground to ~ 5 μm grainsize using an agate mortar, were fabricated by pressing using a pellet die prior to sintering in a 1-atmosphere furnace. In two experiments the 17.5 wt.% of the wollastonite sample was replaced with a 1:1 mixture of $Ca(OH)_2$ + SiO_2 glass, in order to provide a small quantity of water (~ 2 wt.% H_2O in the bulk composition) at experimental conditions to promote the kinetics of Ca-Pv formation (e.g. Gasparik et al., 1994). In all experiments the samples were deformed between two fully dense Al_2O_3 pistons which had 10 μm thick Pt marker foils placed at either end of each sample to allow sample strain to be monitored. Deformation columns were housed within multi-anvil assemblies consisting of a Co-doped MgO octahedron of 7mm edge length, a TiB_2:BN ceramic furnace and MgO inner parts. The pyrophyllite gaskets and ceramic components within the experimental assembly along the X-ray beam path were replaced with rods of low-density boron epoxy to maximise transmission for radiographic imaging and diffraction. Type-D thermocouples with junctions placed adjacent to the samples were used to monitor experimental temperatures.

Experimental assemblies were compressed using secondary anvils with 3mm truncations for pressure generation. 6 x 26 mm TF05 carbide anvils were combined with two X-ray transparent composite anvils placed downstream of the sample to allow collection of angle dispersive diffraction data. These composite anvils consisted of 14mm PCD cubes backed by tungsten carbide spacers which bring the composite cube size up to the 26 mm size of the remaining second-stage anvils. The backing spacers are chamfered to provide a solid cone angle of 20° from the sample position permitting 360° azimuthal diffraction to a 2θ angle of ~ 10° (figure 5). Pressure was applied by gradually increasing the primary ram's oil pressure to 190 ton force over 2-3 hours, corresponding to~ 15-16 GPa as determined using the shift of X-ray diffraction peaks from the Pt marker foils (Matsui et al., 2009). The sample was then gradually heated by applying power to the TiB_2:BN furnace at a rate of between 20-100 K/minute until the target temperature (1150 – 1373K) was achieved. During this heating cycle the wollastonite sample was observed to undergo transformation to Ca-Pv at ~ 1000 K, indicated by an abrupt shortening of the sample (due to large volume change from wollastonite to perovskite structure) and the identification of diffraction rings corresponding to Ca-Pv in subsequent diffraction patterns. After heating all experiments were observed to be at a pressure of 12-13 GPa, which was maintained throughout deformation.

After initial heating the target *PT* conditions were maintained for a minimum of 30 minutes to anneal the samples, and until no diffraction evidence of remnant low pressure $CaSiO_3$ phases was present. Prior to deformation the differential actuators were pre-loaded to an oil pressure of 3 MPa. Sample deformation was commenced by driving both differential actuators, which are controlled by linear displacement transducers, at a fixed rate of 0.5 – 10 μm min^{-1} such that the sample was shortened along an axis parallel to the furnace and the stress-strain data collection loop was commenced. We have observed that after commencing differential ram motion that their pre-load increases to approximately 25% of the main ram's load before motion and sample deformation commences (Nishihara et al., 2020). For these experiments radiographic images of 0.5 – 2 s duration with resolutions of ~ 1 μm were coupled with 180 s sample diffraction patterns using 200x200 μm illumination slits. Diffraction counting times were reduced to 60s when differential actuator velocities of 10 μm min^{-1} were being used to ensure sufficient data were collected at high strain rates. Data collections at constant actuator velocities were repeated for approximately 1 hour to ensure both sample strain rate and stress had reached steady state equilibrium. Multiple strain rates, controlled by three or four differential actuator velocities, were studied in each experiment. All experiments were performed at a single sample temperature of 1150 – 1373K. Following completion of data collection at the final experimental strain rate the sample temperature was quenched by turning off the furnace power and the differential actuators were stopped. The sample was then gradually decompressed at room temperature whilst the actuators were also decompressed over the same time duration in attempt to minimise breakage of the PCD anvils.

Stress-strain data processing

X-ray radiographs were sequentially processed using correlative image processing to determine the relative length change throughout each experiment (e.g. Hunt et al., 2019).

Changes in sample length were subsequently converted into the strain ($\varepsilon = \frac{l-l_0}{l_0}$) experienced by each sample as a function of experimental time. Examples of strain measurement data are provided in figure 6. Strain rates ($\dot{\varepsilon}$ in s^{-1}) were calculated using these strain measurements after steady state was achieved at each subsequent differential actuator velocity. Observed strain rates range between 3x10^{-6} and 2x10^{-4} s^{-1}.

X-ray diffraction data were initially processed using a combination of IPAnalyzer and PDIndexer (Seto et al., 2010), as available at NE7A, to allow evaluation of experiments in real time. Latterly, the diffraction datasets were processed using the newly developed *Continuous Peak Fit* package (Hunt and Fenech, *in prep*, Chen et al., 2021). This package implements a new approach to fitting 2D diffraction (or any other continuous 2D data) by assuming that each diffraction peak, which is normally described in 1D data as a peak function (e.g. a pseudo-Voigt or Gaussian), varies smoothly as a function of azimuth. This description is achieved by fitting each peak parameter (d-spacing, amplitude, half-width etc.) as a Fourier series in azimuthal space. In this case the d-spacing of a single Debye-Scherrer ring was described as:

$$d^{hkl} = a_0^{hkl} + a_1^{hkl}\sin\psi + b_1^{hkl}\cos\psi + a_2^{hkl}\sin 2\psi + b_2^{hkl}\cos 2\psi \qquad \text{(eq.1)}$$

where a_0^{hkl} is the mean d-spacing of the ring, the two first order terms (a_1^{hkl} and b_1^{hkl}) represent the displacement of the centre of the diffraction ring relative to the calibration centre and the second order terms (a_2^{hkl} and b_2^{hkl}) represent the ellipticity of the diffraction ring and contain the information corresponding to the sample's differential strain. This model is fitted sequentially to each of the Debye-Scherrer rings of interest that are not significantly overlapped by peaks from other cell components, in the 2D diffraction pattern. In this case the 110, 200, 211 and 220 peaks of Ca-Pv and the 131, 222, 240, 130, 021, 122 and 140 peaks of olivine samples were fitted using continuous pseudo-Voigt functions, although not all fitted peaks were used for stress evaluations for every experiment. *Continuous Peak Fit* relies on knowledge of the sample-detector geometry as calibrated using an ambient diffraction collection from a CeO_2 standard processed using *Dioptas* (Prescher et al., 2015). The fitting procedure directly provides the lattice strain indicated by each peak accompanied by an uncertainty based on fitting statistics from input of the unprocessed diffraction images in one computational process. A typical example of a fitted Deybe-Scherrer ring for the Ca-Pv 200 at ~ 13 GPa, 1373 K is given in figure 7.

The output models from *Continuous Peak Fit* provide the deviatoric lattice strain and the minimum/maximum d-spacings for each reflection as a function of azimuth, which are evaluated from the second order a_2^{hkl} and b_2^{hkl} Fourier coefficients and trigonometric relations. These parameters can then be used to calculate the differential stress following the approach of Singh et al. (1998), where the relationship between axial stress, lattice strain and azimuthal variations in the peak position is:

$$d_{hkl}\,(\psi) = d_{hkl}^{0}\left[1 + (1 - 3cos^{2}\psi)\,\frac{\sigma}{6\langle G_{hkl}\rangle}\right] \qquad \text{(eq. 2)}$$

In equation 2 d_{hkl} is the *d-spacing* measured as a function of azimuthal angle ψ, d_{hkl}^{0} is the *d-spacing* under hydrostatic pressure, G_{hkl} is the appropriate shear modulus for a given *hkl* orientation and σ is the axial differential stress for that *hkl*.

An approximate evaluation of the differential stress in each sample has been calculated using the maximum and minimum *d-spacing* from fitted models of each diffraction peak combined with either (i) an isotropic shear modulus for olivine or (ii) an appropriately adjusted elastic tensor for Ca-Pv (following the relations in Singh et al., 1998). This approach neglects the effects of crystallographic orientations and elastic anisotropy in olivine samples, but sufficient diffraction peaks are observed that this shouldn't add significant uncertainty to stress estimates. As there are fewer diffraction peaks from Ca-Pv available, and because Ca-Pv has large elastic anisotropy (Kawai and Tsuchiya, 2015), orientation adjusted elastic moduli were used in eq. 2. Throughout stress estimations performed in this paper it was assumed that the isotropic shear modulus of olivine at run conditions (~ 13 GPa and 1150 – 1373 K) was 90 ± 10 GPa, based on recent experimental measurements (Mao et al., 2015). An elastic tensor for Ca-Pv providing values of c_{11}, c_{12} and c_{44} (of 347.9, 158.7 and 179.9 GPa respectively) from the molecular dynamics *ab initio* calculations of Kawai & Tsuchiya (2015) was used to derive differential stresses in perovskite samples. We note that the isotropic adiabatic shear modulus of Ca-Pv reported by Kawai & Tsuchiya (2015) of ~ 155 GPa is significantly larger than those determined in recent ultrasonic interferometry experiments by Greaux et al. (2019) and Thomson et al. (2019) which are ~ 130 and ~ 105 GPa respectively. Thus, the true adiabatic shear modulus of Ca-Pv remains unclear, and the results from Kawai & Tsuchiya (2015) are preferred here because this is the only study to report full c_{ij}'s required to calculate orientation adjusted values of the shear modulus. However, due to these discrepancies, we caution that the differential stresses derived in this study are based on the largest recent estimate of Ca-Pv's shear modulus and may overestimate the true values of differential stress in these experiments by more than 25%. Uncertainties caused by errors in G_{hkl} of Ca-Pv were assumed to be ± 25%, such that estimated stresses incorporate this source of uncertainty, however in several cases the fitting uncertainties dominate. After calculating the apparent stress from each fitted diffraction ring an average differential stress for the olivine and/or Ca-Pv samples was calculated as a weighted mean of all observed stresses. The reported differential stress at each strain rate was calculated as the mean of these weighted averages from each data collection cycle, with uncertainty estimated as two standard deviations. Examples of differential stress measurements are provided in figure 8.

Results.

A summary of conditions, starting materials, measured strain rates and estimated differential stresses from all experiments is provided in Table 1. In all experiments the wollastonite sample material was observed to very rapidly transform into Ca-Pv structure. In the dry experiment diffraction peaks corresponding to Ca-Pv possessed sharp, complete and non-spotty diffraction rings suggesting the Ca-Pv sample had an average grainsize that was large enough to reduce peak broadening, but still small enough that a very large number of grain orientations is being sampled during diffraction. Although this cannot be verified upon recovery, it is assumed samples possess a grainsize between 0.5 – 5 μm, somewhat smaller than those of olivine starting material which were 10-15 μm. In wet experiments diffraction rings from the Ca-Pv were pseudo-continuous, but have a slightly spotty texture implying a larger sample grainsize. Again this cannot be rigorously quantified, but we suggest a similar grainsize to the olivine samples (which have similarly spotty diffraction rings) of ~ 10 μm.

In the single experiment performed on nominally dry starting materials strain was observed to preferentially partition into the Ca-Pv sample relative to olivine, with strain rates in the dry Ca-Pv sample 1.9 – 5.4 times higher than those of the dry olivine sample. Additionally, despite being simultaneously deformed within the same column, the differential stress appears to be significantly lower in the Ca-Pv than olivine in this experiment. As observed in previous studies, dry olivine exhibits a creep strength of 1-2 GPa at strain rates of approximately 1-2 x 10^{-5} s^{-1} (e.g. Li et al., 2006, Kawazoe et al., 2009). In contrast, the simultaneously deforming Ca-Pv sample in our experiments has an apparent creep strength that appears to be an order of magnitude smaller at similar strain rates. This is unusual, as it is normally expected that all samples in a single deforming column should experience the same differential stress, which is clearly not the case in this experiment. In the case where two samples being simultaneously deformed have very different creep strength's it is plausible that the flow in the weaker phase is sufficiently rapid that deformation of the surrounding pressure medium becomes rate-limiting for this sample. That would then cause the differential stress in the weaker sample to be smaller than that in the stronger sample as the pressure medium would be confining the weak sample more strongly. Assuming this is indeed the situation this experiment suggests Ca-Pv is significantly weaker than dry olivine, as indicated by observations of higher strain rate at lower differential stress within the Ca-Pv sample. We note that the differential stress for Ca-Pv in this experiment is derived using the weighted mean stress from 2 Debye-Scherrer rings, as opposed to 5 for olivine samples. In combination with the large uncertainty for Ca-Pv's shear modulus the differential stress estimates for Ca-Pv are relatively larger than those for olivine. Even accounting for this, however, the Ca-Pv appears very significantly weaker than olivine under dry conditions.

Two further experiments were performed using Ca-Pv starting materials containing H_2O provided by 2 wt.% of the starting mix being replaced by a mixture of $Ca(OH)_2$ and SiO_2 glass. This means that these latter deformation experiments are effectively performed in a hydrous environment. Samples of Ca-Pv and olivine simultaneously deformed under hydrous conditions at ~ 13 GPa and 1273 K have more comparable strengths. Strain rates in the hydrous olivine sample were observed to be 1.7 – 2.3 times higher than those for Ca-Pv, and differential stress appears to be similar in both samples at strain rates of 2-4 x 10^{-5} s^{-1}, with olivine becoming relatively weaker at lower strain rates. The final experiment was performed on a solitary sample of Ca-Pv at a temperature of 1373 K and under hydrous conditions. This solitary Ca-Pv experiment was performed as the strain rate of Ca-Pv samples in previous experiments had been high, and including only Ca-Pv permitted a longer initial sample length. At equivalent differential stress increasing temperature weakens the Ca-Pv sample, which was observed to strain faster than at 1273K (figure 9).

Discussion.

The presented experiments and data analysis approach using the *Continuous Peak Fit* package, as described above, demonstrate the capabilities of the D111 at KEK NE7A for deformation experiments at mantle conditions. Experiments are reported with strain rates as low as ~ 3-7 x 10^{-6} s^{-1} with differential stresses of ~ 20 ± 10 MPa in hydrous olivine samples. Equally, anhydrous olivine samples deformed at similar strain rates were observed to support differential stress of 1300 ± 70 MPa at a strain rate of ~ 5 x 10^{-6} s^{-1}. These observations for both hydrous and anhydrous samples overlap published rheological properties for wet and dry olivine respectively (e.g. Ohuchi et al., 2017, Kawazoe et al., 2009), verifying the capabilities of the D111 to perform rheological experiments similar to other devices available (e.g. d-DIA and RDA) at synchrotron beamlines worldwide. The apparent slope of data for strain rate vs. differential stress suggests that hydrous samples of olivine may be deforming in the diffusion creep regime ($n < 1$) whilst anhydrous samples are deforming in dislocation creep ($n > 3$) in the current study (figure 9, equation 3).

Observations on Ca-Pv samples, although preliminary, allow some initial observations of its rheological properties at mantle *PT* conditions. Across all three experiments, in both dry and hydrous sample conditions, the maximum average differential stress observed in Ca-Pv samples was 430 ± 129 MPa. Whilst these stress estimates are subject to large errors in part due to the uncertainty in the elastic tensor of Ca-Pv, it is unambiguous that they are low compared with other high-pressure silicate phases at equivalent strain rates. In the anhydrous experiment it appeared, comparing both differential stresses and observed sample strain rates, that Ca-Pv may be more than 1 order of magnitude weaker than coexisting olivine. Taken absolutely at face value these observations point to Ca-Pv being substantially weaker than dry olivine (figure 9). However, it is noted that Ca-Pv samples are synthesised *in-situ* and their grainsize is not known accurately. Whilst the diffraction characteristics described above imply Ca-Pv samples probably have a grainsize of 0.5-5 μm which is smaller than that of the olivine starting material, and is potentially sufficiently small to make it anomalously weak. Since the spontaneous amorphization of Ca-Pv during decompression prevents a rigorous grainsize measurement this could not be verified, and it was in order to try and study Ca-Pv samples with larger average grainsizes that subsequent experiments were performed under hydrous conditions. Whilst the slight spottiness of Ca-Pv diffraction rings in hydrous conditions suggested the success of this approach in creating coarser perovskite samples, it also induced a significant hydrolytic weakening in coexisting olivine (e.g. Mei and Kohlstedt, 2002a, 2002b). However, the presence of hydrogen did not appear to weaken Ca-Pv in a similar manner as hydrous Ca-Pv deforming at 1273K (123 K above the dry experiment) appeared to be stronger than that under dry conditions. We assume this increase in strength is the expression of increased sample grainsize. The strength of Ca-Pv under hydrous conditions did reduce with temperature increasing from 1273 to 1373 K, as is expected. A brief inspection of the slope of data for all Ca-Pv sample in figure 9 suggests in all three experiments Ca-Pv was deforming in a diffusion creep regime at run conditions.

In order to consider this further the strain rate vs. stress data for Ca-Pv were fitted to a thermally activated creep flow law of the form:

$$\dot{\varepsilon} = A\frac{\sigma^n}{d^m}exp\left(-\frac{Q}{RT}\right) \qquad \text{(eq. 3)}$$

Where *A* is the constant of proportionality, *n* is the dimensionless stress dependence, *d* is the grainsize and *m* is the dimensionless grainsize dependence, *Q* is the activation energy, *R* is the universal gas constant and *T* is the temperature. By utilising a flow law of this form we are inherently assuming that the presence (and concentration) of water has no effect on the creep strength of Ca-Pv. Whilst this is a significant, and unjustified, assumption our qualitative observations all suggest Ca-Pv is relatively weak compared with other silicates irrespective of the presence or lack of water in our experiments, thus it is arguably not the most significant component in controlling Ca-Pv's creep strength. Additionally, by making this assumption estimates for other flow law parameters can be obtained. Finally, in order to fit the data for Ca-Pv we assumed that wet experiments had a grainsize of 10 μm and that the grainsize dependence of Ca-Pv's creep is fixed at *m* = 2, that is, we assume Nabarro-Herring creep. Making these assumptions and performing a weighted regression we obtain values of *Q* and *n* of 364 kJ mol^{-1} and 1.28 respectively, with an inferred grainsize in the dry experiment of 0.6 μm. If we assume Coble creep (*m*=3) the dry grainsize changes to 0.7 μm. This predicted activation energy is entirely dependent on data from the two wet experiments and is not strongly influenced by our assumptions about the effect of water on creep strength or the exact grainsize in the experiments. Additionally, an activation energy of 364 kJ mol^{-1} is very similar to the activation energy for Si diffusion in bridgmanite (~ 330-350 kJ mol^{-1}, Dobson et al., 2008, Yamazaki et al., 2000) and as such appears both reasonable and fairly robust. This implies the fitted value for *n*, of 1.28, and the relative grainsizes of wet/dry experiments are also likely to be reliable since the exact grainsizes are effectively an adjustable parameter, such that we conclude Ca-Pv in these experiments is deforming in a diffusion creep regime.

Irrespective of Ca-Pv's deformation regime in experiments here, comparison with stress-strain data from similar experiments allows a direct comparison of its strength with additional mantle silicates. Ringwoodite samples deformed using the d-DIA at ~ 17 GPa and 1300-1700 K sustain similar differential stress (130 – 560 MPa) at strain rates of 10^{-5} s^{-1} (figure 9, Kawazoe et al., 2016). This suggests that Ca-Pv and ringwoodite possess broadly similar rheological properties. Comparisons with data for wadsleyite (Kawazoe et al., 2010, Hustoft et al., 2013) and/or bridgmanite (Girard et al., 2016) samples suggests Ca-Pv is more than an order of magnitude weaker than either of these materials at the strain rates probed in this study (figure 9). Such comparisons only provide a qualitative understanding of relative strengths of mantle phases, but suggest that Ca-Pv may be capable of inducing rheological contrasts at deep Earth conditions. During subduction, the similar properties of Ca-Pv and ringwoodite might suggest that basaltic and harzburgitic slab assemblages retain similar strengths throughout subduction within the upper mantle and transition zone. However, after entry to the lower mantle the rheology of these lithologies may significantly diverge. The rheological behaviour of subducting basalts, which contain up to 30 vol.% Ca-Pv (Perrillat et al., 2006), may be controlled by interconnected grains of this phase whilst harzburgite assemblages contain > 90% bridgmanite (Ishii et al., 2019). In this situation the strength contrast of Ca-Pv and bridgmanite may cause downwelling slabs to delaminate and could promote slab stagnation in the upper/lower mantle boundary region (e.g. Fukao et al., 2013). Additionally, in more fertile ultramafic assemblage throughout the lower mantle, both Ca-Pv and MgO may act as weak phases coexisting with bridgmanite and together may constitute > 20 vol.% of phase assemblages (Perrillat et al., 2006). If these grains of Ca-Pv and MgO are sufficient to generate an interconnected network within a bridgmanite matrix this will allow strain partitioning into these phases and cause and overall weakening of peridotitic assemblages in the lower mantle. Such rheological contrasts between depleted and fertile components of an ultramafic lower mantle assemblage may allow generation of 3-dimensionally distributed domains of rigid materials (e.g. BEAMs, Ballmer et al., 2017). Additional studies of the rheological properties of Ca-Pv in relation to those of lower mantle materials are required to further investigate these possibilities.

Conclusions.

A D111 deformation multi-anvil press has been successfully installed at beamline NE7A of KEK and utilised to performed deformation experiments at controlled strain rates of 10^{-6} to 10^{-4} s^{-1} at mantle pressure and temperature conditions. In this study we have demonstrated the capabilities of the D111 geometry using controlled strain rate experiments of Ca-Pv and olivine samples under both wet and dry conditions with sample strain rates between 3×10^{-6} s^{-1} and 2×10^{-4} s^{-1} occurring in response to differential stresses of ~ 20 to 1760 MPa. Preliminary data suggest that Ca-Pv is up to 1 order of magnitude weaker compared with other deep mantle silicate minerals including olivine, wadsleyite and bridgmanite and may strongly influence the geodynamics of the Earth's deep mantle.

The stability of the Kawai 6/8 geometry, which forms the basis of the D111 deformation press, means that *PT* conditions at controlled strain rates may be extended significantly beyond those achievable in other existing deformation geometries, such as the d-DIA and Rotational Drickamer. To date experiments have been performed at conditions up to ~ 27 GPa and 1700 K, to investigate the creep strength of Earth-forming materials including hcp-structured iron, ringwoodite and bridgmanite (Nishihara et al., 2020). Further developments, including use of harder anvil materials (e.g. Yamazaki et al., 2019) and new X-ray transparent ceramic components (e.g. Xie et al., 2020a, 2020b, Xu et al., 2020) should allow additional expansion of the accessible *PT* conditions using this deformation geometry.

Acknowledgements.

We thank two anonymous reviews for their comments and Taku Tsuchiya for his editorial handling of this paper. We acknowledge the support of UKRI grant NE/P017657/1 and grants 15H05827, 15H03749, 19H00723 and 18H05232 from the Japan Society for Promotion of Science.

References.

Ballmer, M. D., Houser, C., Hernlund, J. W., Wentzcovitch, R. M., & Hirose, K. (2017). Persistence of strong silica-enriched domains in the Earth's lower mantle. *Nature Geoscience*, *10*(3), 236–240. http://doi.org/10.1038/ngeo2898

Chen, Y., Clark, S. J., Collins, D. M., Marussi, S., Hunt, S. A., Fenech, D. M., et al. (2021). Correlative synchrotron X-ray imaging and diffraction of directed energy deposition additive manufacturing. *Acta Materialia*, *209*, 116777.

Dobson, D. P., Dohmen, R., & Wiedenbeck, M. (2008). Self-diffusion of oxygen and silicon in $MgSiO_3$ perovskite. *Earth and Planetary Science Letters*, *270*(1-2), 125–129.

Dobson DP, Hunt SA and Müller HJ. (2012) Slotted Carbide Anvils: Improved X-ray Access for Synchrotron Multi-Anvil Experiments. High Pressure Research, 32, 532-536, 2012.

Farmer, N., Rushmer, T., Wykes, J., & Mallmann, G. (2020). The Macquarie Deformation-DIA facility at the Australian Synchrotron: A tool for high-pressure, high-temperature experiments with synchrotron radiation. *Review of Scientific Instruments*, *91*(11), 114501.

Fukao, Y., & Obayashi, M. (2013). Subducted slabs stagnant above, penetrating through, and trapped below the 660 km discontinuity. *Journal of Geophysical Research B: Solid Earth*, *118*(11), 5920–5938. http://doi.org/10.1002/2013JB010466

Gasparik, T., Wolf, K., and Smith, C. M. (1994). Experimental determination of phase relations in the $CaSiO_3$ system from 8 to 15 GPa. *American Mineralogist 79*(11-12), 1219-1222.

Girard, J., Amulele, G., Farla, R., Mohiuddin, A., & Karato, S.-I. (2016). Shear deformation of bridgmanite and magnesiowüstite aggregates at lower mantle conditions. *Science*, *351*(6269), 144–147. http://doi.org/10.1126/science.aad3113

Gréaux, S., Irifune, T., Higo, Y., Tange, Y., Arimoto, T., Liu, Z., & Yamada, A. (2019). Sound velocity of $CaSiO_3$ perovskite suggests the presence of basaltic crust in the Earth's lower mantle. *Nature*, *565*(7738), 218–221. http://doi.org/10.1038/s41586-018-0816-5

Guignard, J., & Crichton, W. A. (2015). The large volume press facility at ID06 beamline of the European synchrotron radiation facility as a High Pressure-High Temperature deformation apparatus. *Review of Scientific Instruments*, *86*(8), 085112.

Handy, M. R. (1994). Flow laws for rocks containing 2 nonlinear viscous phases. *Journal of Structural Geology*, *16*(12), 1727. http://doi.org/10.1029/2002JB001833/full

van der Hilst, Complex morphology of subducted lithosphere in the mantle beneath the Tonga trench. Nature 374, 154-157 (1995)

Hunt, S.A. Dobson, D.P. Li, L. McCormack, R.J. Vaughan, M.T. Weidner, D.J. & Whitaker, M. Deformation T-Cup: A new apparatus for high temperature, controlled strain-rate deformation experiments at pressures in excess of 18 GPa. Rev. Sci. Instr. 85, 085103, 2014.

Hunt, SA and Dobson DP. Modified anvil design for improved reliability in DT-cup experiments. Rev. Sci. Instr., 88, 126106, 2017.

Hunt, S. A., Whitaker, M. L., Bailey, E., Mariani, E., Stan, C. V., & Dobson, D. P. (2019). An experimental investigation of the relative strength of the silica polymorphs quartz, coesite, and stishovite. *Geochemistry, Geophysics and Geosystems*, *20*(4), 1975–1989.

Hustoft, J., Amulele, G., Ando, J. I., Otsuka, K., Du, Z., Jing, Z., & Karato, S.-I. (2013). Plastic deformation experiments to high strain on mantle transition zone minerals wadsleyite and ringwoodite in the rotational Drickamer apparatus. *Earth and Planetary Science Letters*, *361*, 7–15.

T. Irifune, W. Utsumi, and T. Yagi. Use of a new diamond composite for multianvil high-pressure apparatus. Proc. Jpn. Acad., 68B, 161-166 (1992) DOI: 10.2183/pjab.68.161

Ishii, T., Kojitani, H., & Akaogi, M. (2019). Phase relations of Harzburgite and MORB up to the uppermost lower mantle conditions: Precise comparison with Pyrolite by multisample cell high-pressure experiments with implication to dynamics of subducted slabs. *Journal of Geophysical Research: Solid Earth*, *124*(4), 3491-3507.

Ito, E., et al. "Theory and practice-multianvil cells and high-pressure experimental methods." *Treatise on geophysics 2* (2007): 197-230.

Kawai, N., and Endo, S. (1970) The generation of ultrahigh hydrostatic pressure by a split sphere apparatus. Reviews of Scientific Instruments, 41, 425-428.

Kawai, N., Togaya, M. and Onodera, A. 1973. New device for pressure-vessels. Proc. Jpn. Acad, 49(8): 623–626.

Kawai, K., & Tsuchiya, T. (2015). Small shear modulus of cubic $CaSiO_3$ perovskite. *Geophysical Research Letters*, *42*(8), 2718–2726. http://doi.org/10.1002/2015GL063446

Kawazoe, T., Karato, S.-I., Otsuka, K., Jing, Z., & Mookherjee, M. (2009). Shear deformation of dry polycrystalline olivine under deep upper mantle conditions using a rotational Drickamer apparatus (RDA). *Physics of the Earth and Planetary Interiors*, *174*(1-4), 128–137. http://doi.org/10.1016/j.pepi.2008.06.027

Kawazoe, T., Karato, S.-I., Ando, J. I., Jing, Z., Otsuka, K., & Hustoft, J. W. (2010). Shear deformation of polycrystalline wadsleyite up to 2100 K at 14-17 GPa using a rotational Drickamer apparatus (RDA). *Journal of Geophysical Research B: Solid Earth*, *115*(8), B08208. http://doi.org/10.1029/2009JB007096

Kawazoe, T., Nishihara, Y., Ohuchi, T., Miyajima, N., Maruyama, G., Higo, Y., et al. (2016). Creep strength of ringwoodite measured at pressure–temperature conditions of the lower part of the mantle transition zone using a deformation–DIA apparatus. *Earth and Planetary Science Letters*, *454*, 10–19. http://doi.org/10.1016/j.epsl.2016.08.011

Karato, S-i. On the separation of crustal component from subducted oceanic lithosphere near the 660 km discontinuity. Phys. Earth Planet. Inter., 99, 103-111, 1997.

Karato, S-I and Rubie, DC. Toward an experimental study of deep mantle rheology: A new multianvil sample assembly for deformation studies under high pressures and temperatures. J. Geophys. Res., 102, 20111-20122, 1997.

Kesson, S. E., Fitz Gerald, J. D., & Shelley, J. M. (1998). Mineralogy and dynamics of a pyrolite lower mantle. *Nature*, *393*(6682), 252–255. http://doi.org/10.1038/30466

Krusky TM, Li, J-H, Tucker RD. The Archean Dongwanzi Ophiolite Complex, North China Craton: 2.505-Billion-Year-Old Oceanic Crust and Mantle. Science, 292, 1142-1145. DOI: 10.1126/science.1059426

Li, L. I., Weidner, D., Raterron, P., Chen, J., Vaughan, M., Mei, S., & Durham, B. (2006). Deformation of olivine at mantle pressure using the D-DIA. *European Journal of Mineralogy*, *18*(1), 7–19.

Li, L., Raterron, P., Weidner, D.J. and Chen, J. (2003) Olivine flow mechanisms at 8 GPa. Physics of the Earth and Planetary Interiors, 138, 113-129.

Liebermann, RC. Multi-anvil, high pressure apparatus: a half-century of development and progress. High Pressure Research, 31, 493-532, 2011.

Liu, L.-G., & Ringwood, A. E. (1975). Synthesis of a perovskite-type polymorph of $CaSiO_3$. *Earth and Planetary Science Letters*, *28*(2), 209–211. http://doi.org/10.1016/0012-821X(75)90229-0

Mao, Z., Fan, D., Lin, J.-F., Yang, J., Tkachev, S. N., Zhuravlev, K., & Prakapenka, V. B. (2015). Elasticity of single-crystal olivine at high pressures and temperatures. *Earth and Planetary Science Letters*, *426*, 204–215.

Matsui, M., Ito, E., Katsura, T., Yamazaki, D., Yoshino, T., Yokoyama, A., & Funakoshi, K. I. (2009). The temperature-pressure-volume equation of state of platinum. *Journal of Applied Physics*, *105*(1), 013505.

Mei, S., & Kohlstedt, D. L. (2000). Influence of water on plastic deformation of olivine aggregates 1. Diffusion creep regime. *Journal of Geophysical Research B: Solid Earth*, *105*(B9), 21457–21469.

Mei, S., & Kohlstedt, D. L. (2000). Influence of water on plastic deformation of olivine aggregates 2. Dislocation creep regime. *Journal of Geophysical Research B: Solid Earth*, *105*(B9), 21471–21481.

Nishihara, Y., Yamazaki, D., Tsujino, N., Doi, S., Kubo, T., Imamura, M., & Yoshino, T. (2020). Studies of deep earth rheology based on high-pressure deformation experiments using d111-type apparatus. *Review of High Pressure Science and Technology/Koatsuryoku No Kagaku to Gijutsu*, *30*(2), 78–84.

Nishiyama N, Wang Y, Sanehira T, Irifune T & Rivers ML. (2008) Development of the Multi-anvil Assembly 6-6 for DIA and D-DIA type high-pressure apparatuses, High Pressure Research, 28:3, 307-314, DOI: 10.1080/08957950802250607

Ohuchi, T., Kawazoe, T., Higo, Y., & Suzuki, A. (2017). Flow behavior and microstructures of hydrous olivine aggregates at upper mantle pressures and temperatures. *Contributions to Mineralogy and Petrology*, *172*(8), 1–26.

Perrillat, J. P., Ricolleau, A., Daniel, I., Fiquet, G., Mezouar, M., Guignot, N., & Cardon, H. (2006). Phase transformations of subducted basaltic crust in the upmost lower mantle. *Physics of the Earth and Planetary Interiors*, *157*(1-2), 139-149.

Prescher, C., & Prakapenka, V. B. (2015). DIOPTAS: a program for reduction of two-dimensional X-ray diffraction data and data exploration. *High Pressure Research*, *35*(3), 223–230.

Seto, Y. (2010). Development of a software suite on X-ray diffraction experiments. *The Review of High Pressure Science and Technology*, *20*, 269–276.

O. Shimomura, S. Yamaoka, T. Yagi, M. Wakatsuki, K. Tsuji, H. Kawa- mura, N. Hamaya, O. Fukuoga, K. Aoki, and S. Akimoto, in Solid State Physics Under Pressure, edited by S. Minomura. Terra Scientific, Tokyo, Japan, 1985, pp. 351–356.

Singh, A. K., Balasingh, C., Mao, H.-K., Hemley, R. J., & Shu, J. (1998). Analysis of lattice strains measured under nonhydrostatic pressure. *Journal of Applied Physics*, *83*(12), 7567–7575.

Thomson A.R., Crichton W.A., Brodholt J.P., Wood I.G., Siersch N.C., Muir J., Dobson D.P. and Hunt S.A. Seismic velocities of $CaSiO_3$ perovskite can explain LLSVPs in Earth's lower mantle. Nature 572, pages643–647 (2019)

Tsujino, N., Nishihara, Y., Yamazaki, D. et al. Mantle dynamics inferred from the crystallographic preferred orientation of bridgmanite. Nature 539, 81–84 (2016). https://doi.org/10.1038/nature19777

Wang, Y., & Weidner, D. J. (1994). Thermoelasticity of $CaSiO_3$ perovskite and implications for the lower mantle. *Geophysical Research Letters*, *21*(10), 895–898. http://doi.org/10.1029/94GL00976

Wang, Y., Durham, W. B., Getting, I. C., & Weidner, D. J. (2003). The deformation-DIA: A new apparatus for high temperature triaxial deformation to pressures up to 15 GPa. *Review of Scientific Instruments*, *74*(6), 3002–3011.

Wang, Y., Rivers, M., Sutton, S., Nishiyama, N., Uchida, T., & Sanehira, T. (2009). The large-volume high-pressure facility at GSECARS: A "Swiss-army-knife" approach to synchrotron-based experimental studies. *Physics of the Earth and Planetary Interiors*, *174*(1-4), 270–281.

Xie, L., Yoneda, A., Xu, F., Higo, Y., Wang, C., Tange, Y., et al. (2020a). Boron–MgO composite as an X-ray transparent pressure medium in the multi-anvil apparatus. *Review of Scientific Instruments*, *91*(4), 043903.

Xie, L., Yoneda, A., Liu, Z., Nishida, K., & Katsura, T. (2020b). Boron-doped diamond synthesized by chemical vapor deposition as a heating element in a multi-anvil apparatus. *High Pressure Research*, *40*(3), 369–378.

Xu, F., Xie, L., Yoneda, A., Guignot, N., King, A., Morard, G., & Antonangeli, D. (2020). TiC-MgO composite: an X-ray transparent and machinable heating element in a multi-anvil high pressure apparatus. *High Pressure Research*, *40*(2), 257–266.

Yamazaki, D., Ito, E., Yoshino, T., Tsujino, N., Yoneda, A., Gomi, H., et al. (2019). High-pressure generation in the Kawai-type multianvil apparatus equipped with tungsten-carbide anvils and sintered-diamond anvils, and X-ray observation on $CaSnO_3$ and $(Mg,Fe)SiO_3$. *Comptes Rendus Geoscience*, *351*(2-3), 253–259. http://doi.org/10.1016/j.crte.2018.07.004

Yamazaki, D., Kato, T., Yurimoto, H., Ohtani, E., & Toriumi, M. (2000). Silicon self-diffusion in $MgSiO_3$ perovskite at 25 GPa. *Physics of the Earth and Planetary Interiors*, *119*(3-4), 299–309.

Tables.

Table 1: Summary of experimental run conditions and results from deformation

expt	P (GPa)	T (K)	starting materials	Sample *hkls used for stress*	Deformation velocity (μm min^{-1})	$\dot{\varepsilon}$ (s^{-1})	±	σ (MPa)	±
A (dry)	13	1150	$CaSiO_3$	Ca-Pv *200, 110*	4	1.91×10^{-5}	*4.48×10^{-5}*	116	*24*
					1	2.51×10^{-5}	*1.83×10^{-5}*	109	*27*
					10	1.83×10^{-4}	*8.12×10^{-5}*	260	*99*
			$(Mg_{1.8}Fe_{0.2})SiO_4$	olivine *021, 122, 130, 140, 222*	4	1.00×10^{-5}	*1.18×10^{-5}*	1480	*400*
					1	4.65×10^{-6}	*5.8×10^{-6}*	1300	*70*
					10	4.87×10^{-5}	*1.93×10^{-5}*	1760	*240*
B (wet)	13	1273	$CaSiO_3$ + 2wt.% H_2O	Ca-Pv *200, 110, 211*	4	2.54×10^{-5}	*3.1×10^{-6}*	430	*129*
					1	7.72×10^{-6}	*2.4×10^{-6}*	164	*23*
					0.5	3.28×10^{-6}	*4.3×10^{-6}*	132	*25*
			Mg_2SiO_4	olivine *131, 222, 130, 021, 122, 140*	4	4.27×10^{-5}	*1.2×10^{-6}*	396	*44*
					1	1.58×10^{-5}	*1.1×10^{-6}*	92	*25*
					0.5	7.67×10^{-6}	*8.6×10^{-7}*	19	*11*
C (wet)	13	1373	$CaSiO_3$ + 2wt.% H_2O	Ca-Pv *200, 110, 220*	4	6.42×10^{-5}	*9.2×10^{-6}*	91	*79*
					1	2.04×10^{-5}	*1.7×10^{-6}*	52	*23*
					0.5	9.98×10^{-6}	*1.3×10^{-6}*	68	*13*
					10	1.73×10^{-4}	*1.02×10^{-5}*	316	*177*

Figure captions.

Figure 1: Schematic illustrations showing the geometries, hydrostatic compression directions (white arrows) and differential deformation (black arrows) of various high-pressure experimental apparatus. The (a) DIA 6/8 and (b) Kawai 6/8 (which may also be named the “111 6/8”) geometries both utilise 6 primary anvils in combination with 8 secondary truncated cubic anvils and an octahedral pressure medium to perform hydrostatic experiments, with the significant difference being the wedge-shaped primaries and rotated orientation of the secondary anvils in the Kawai 6/8 geometry. The (c) d-DIA geometry utilises 6 secondary anvils and a cubic pressure medium to apply differential strain in the vertical direction whereas (d) the D-dia 6/8 geometry uses the same primary anvils to deform an octahedral pressure medium within 8 secondary anvils, with differential strain loading the pyrophyllite gaskets. (e) and (f) show two alternative cross sections of the D111 / D-T-cup drawn (e) parallel and (f) perpendicular to the incident X-ray beam. The D111/D-T-cup geometry uses a Kawai-type geometry of primary wedges with differential strain applied onto two opposing anvil truncations along the 111 axis of the secondary anvil set.

Figure 2: (a) a schematic of the D111 guide block at NE7A of KEK depicting the Kawai 6/8 geometry arrangement within a split confining ring and position of the differential deformation actuators. (b) A view of D111 module consisting of the split confining ring (1) and lower differential actuator (2) next to the MAX-III load frame on NE7A taken from an upstream position and showing the direction of the synchrotron X-ray beam in relation to the press.

Figure 3: A schematic of beamline layout on NE7A at KEK when setup for monochromatic diffraction experiments using the D111 module, including the position of the X-ray

collimation slits, radiographic CCD/CMOS camera and image plate detector and the motorized linear stages used to switch between imaging and diffraction modes.

Figure 4: Pressure and temperature conditions of deformation experiments performed using the D111 at NE7A up until now, plotted alongside relevant phase relations. Samples studied are indicated by symbols as follows: circles = fcc-iron, large white stars = Ca-Pv/olivine (this study), small grey stars = olivine, dark grey triangles = ringwoodite, squares = bridgmanite.

Figure 5: (a) WC spacers for monochromatic diffraction, consisting of 3 variously shaped trapezoidal WC spacers with cone cut-out for diffraction, adjacent to a fully assembled composite anvil consisting 3 spacers combined with a 14mm PCD cube. (b) An example X-ray diffraction pattern collected using two downstream composite anvils collected from a Ca-Pv sample at ~ 13 GPa and 1273 K. The direct beam can be observed as a small spot in the centre of the diffraction rings within the Pb beamstop that was attached to the image plate detector, and Debye-Scherrer rings extend to 10° 2 theta (equivalent to a d-spacing of ~ 1.17 Å using monochromatic X-rays of 0.2066 Å). The more intense stripe inclined from the lower left to upper right is due to the increased X-ray transmission through the anvil gap.

Figure 6: (a) length of Ca-Pv (filled circles) and olivine (filled squares) at 13 GPa and 1273K under hydrous conditions as a function of time throughout deformation, as derived from radiographic images, and coloured by the differential ram velocity (as annotated). (b) the strain of Ca-Pv and olivine samples as a function of time throughout the same experiment. Small symbols were not used to derive strain rates (annotated and indicated by dashed lines) as these had not yet reached steady state after change in ram velocities.

Figure 7: Example of the fitted output from *Continuous Peak Fit* for wet Ca-Pv 200 at 13 GPa and 1373K. The left-hand panel plots the raw data as a function of diffraction azimuth and 2θ (both in degrees). Regions of the data that are white are masked due to large intensity changes in the anvil gap, which hampers successful fitting of the diffraction rings. The middle panel plots the calculated model of the fitted peak, with the black dashed line indicating the model peak position. The right-hand panel plots the residual misfit between the raw data and the fitted peak model. All panels are coloured by intensity, indicated by the adjacent colour bars (colour figure provided as supplementary figure).

Figure 8: Examples of stress data collected throughout (a) experiment B for hydrous olivine and (b) experiment C for hydrous Ca-Pv.

Figure 9: Summary of the creep strength of Ca-Pv (large, coloured circles) and olivine samples (large, coloured squares), plotted as strain rate vs. differential stress, as observed in experiments performed using the D111 at KEK in this study. Uncertainties in observed strain rates and differential stresses, as reported in Table 1, are plotted and in some cases are smaller than the symbol size. There are plotted alongside creep strength data for other

silicate minerals from similar experiments using D-dia or Rotational Drickamer apparatuses for comparison; white triangles = creep strength data for ringwoodite (Kawazoe et al., 2016), green triangles = wadsleyite (Kawazoe et al., 2010, Hustoft et al., 2013), light green squares = bridgmanite (Girard et al., 2016), light green diamonds = wet olivine (Ohuchi et al., 2017), light blue diamonds = dry olivine (Kawazoe et al., 2009).

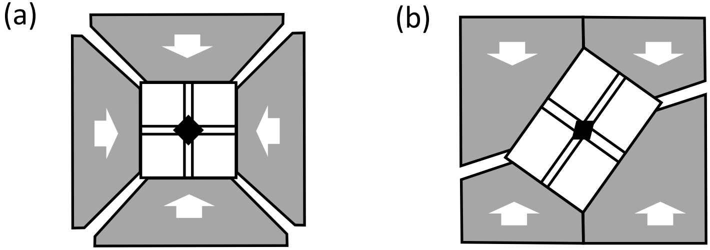

DIA 6/8 Kawai 6/8

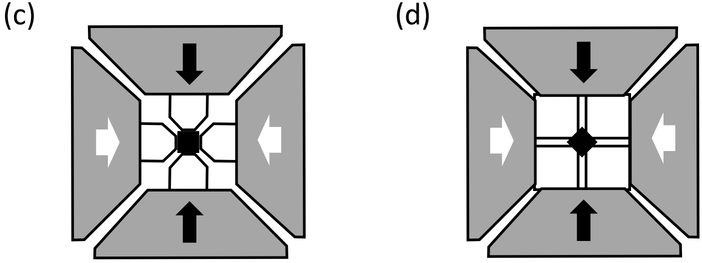

d-DIA d-DIA 6/8

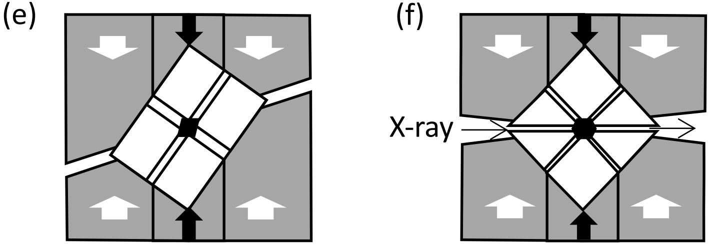

D111 / D-T-cup D111 / D-T-cup

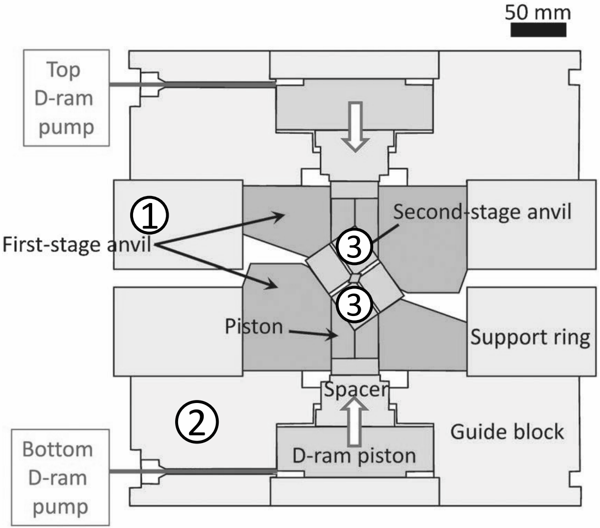
50 mm
Top D-ram pump
①
First-stage anvil
Second-stage anvil
③
③
Piston
Support ring
Spacer
②
Guide block
Bottom D-ram pump
D-ram piston

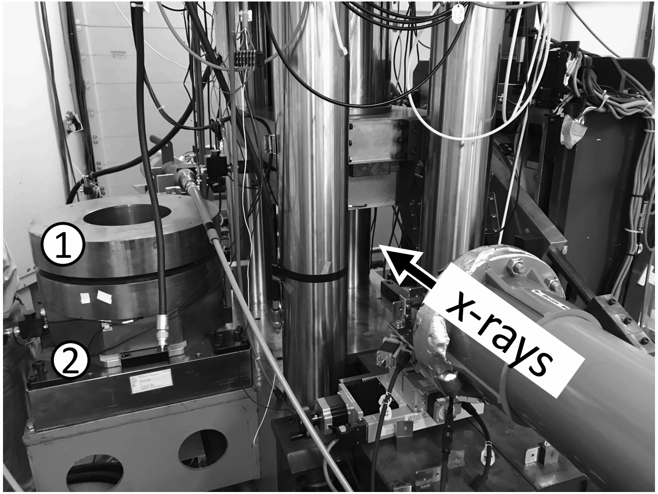
①
②
x-rays

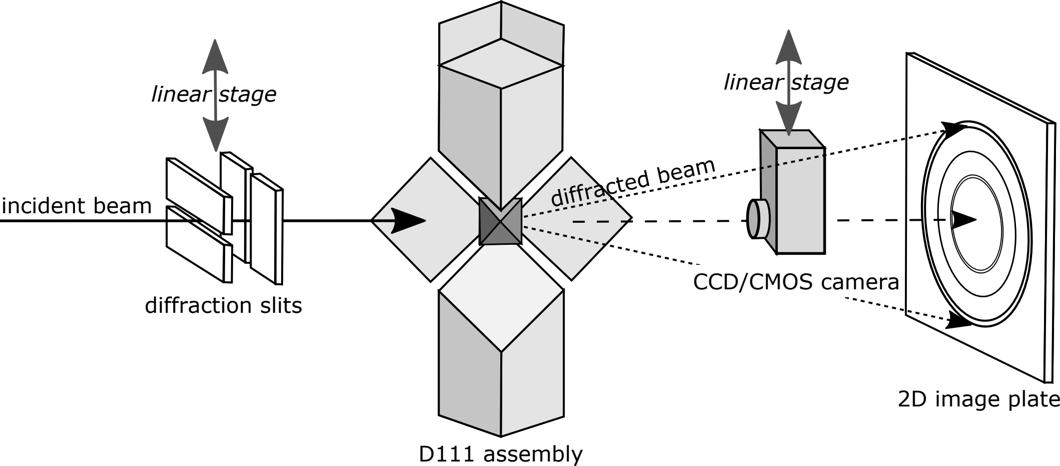
linear stage
incident beam
diffraction slits
D111 assembly
diffracted beam
linear stage
CCD/CMOS camera
2D image plate

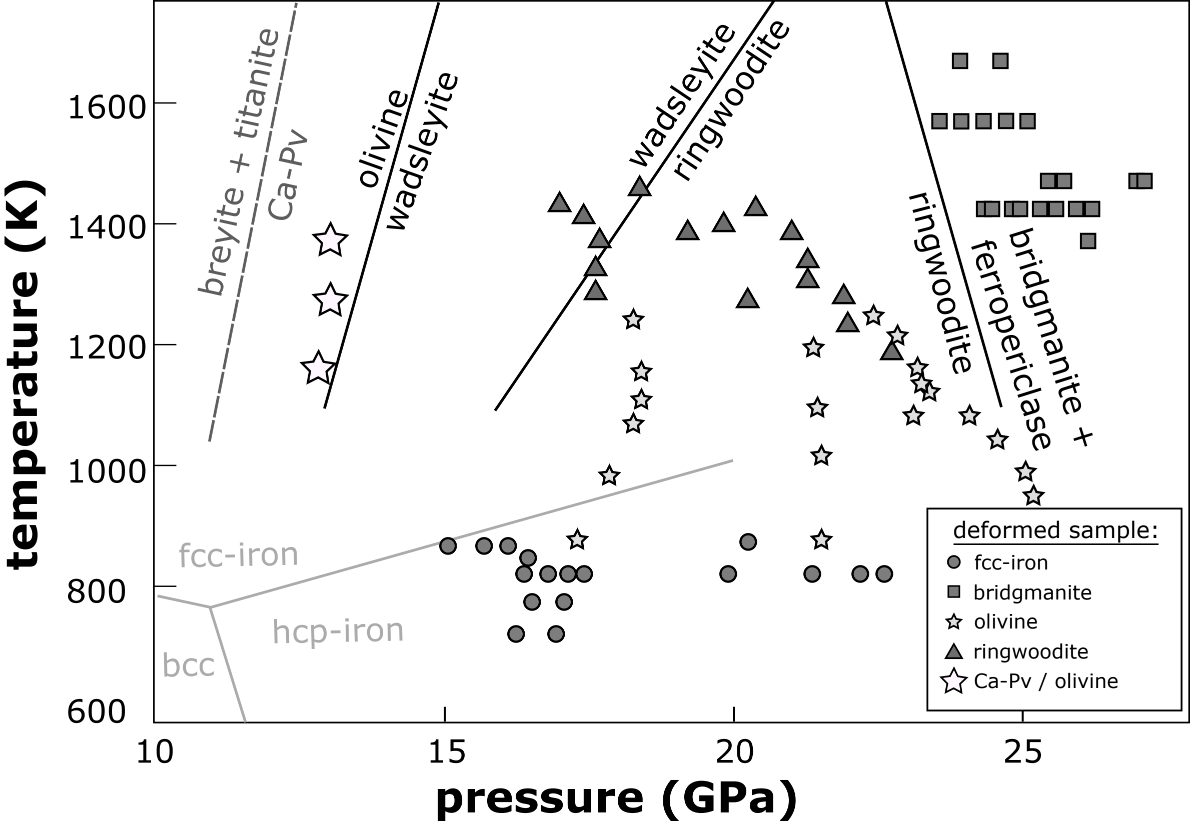
breyite + titanite
Ca-Pv
olivine
wadsleyite
wadsleyite
ringwoodite
ringwoodite
bridgmanite + ferropericlase
fcc-iron
hcp-iron
bcc
deformed sample:
● fcc-iron
■ bridgmanite
☆ olivine
▲ ringwoodite
☆ Ca-Pv / olivine
temperature (K)
600
800
1000
1200
1400
1600
pressure (GPa)
10
15
20
25

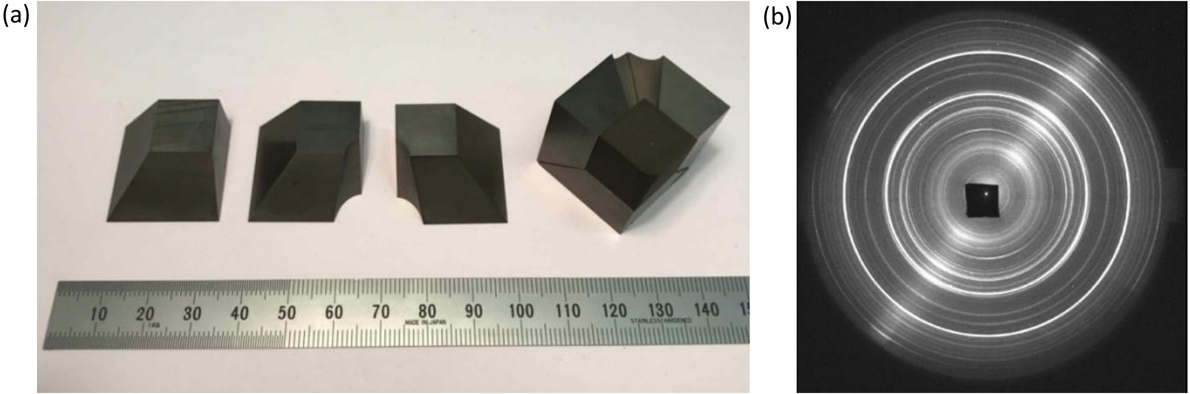
(a)
(b)
10 20 30 40 50 60 70 80 90 100 110 120 130 140
MADE IN JAPAN
STAINLESS HARDENED

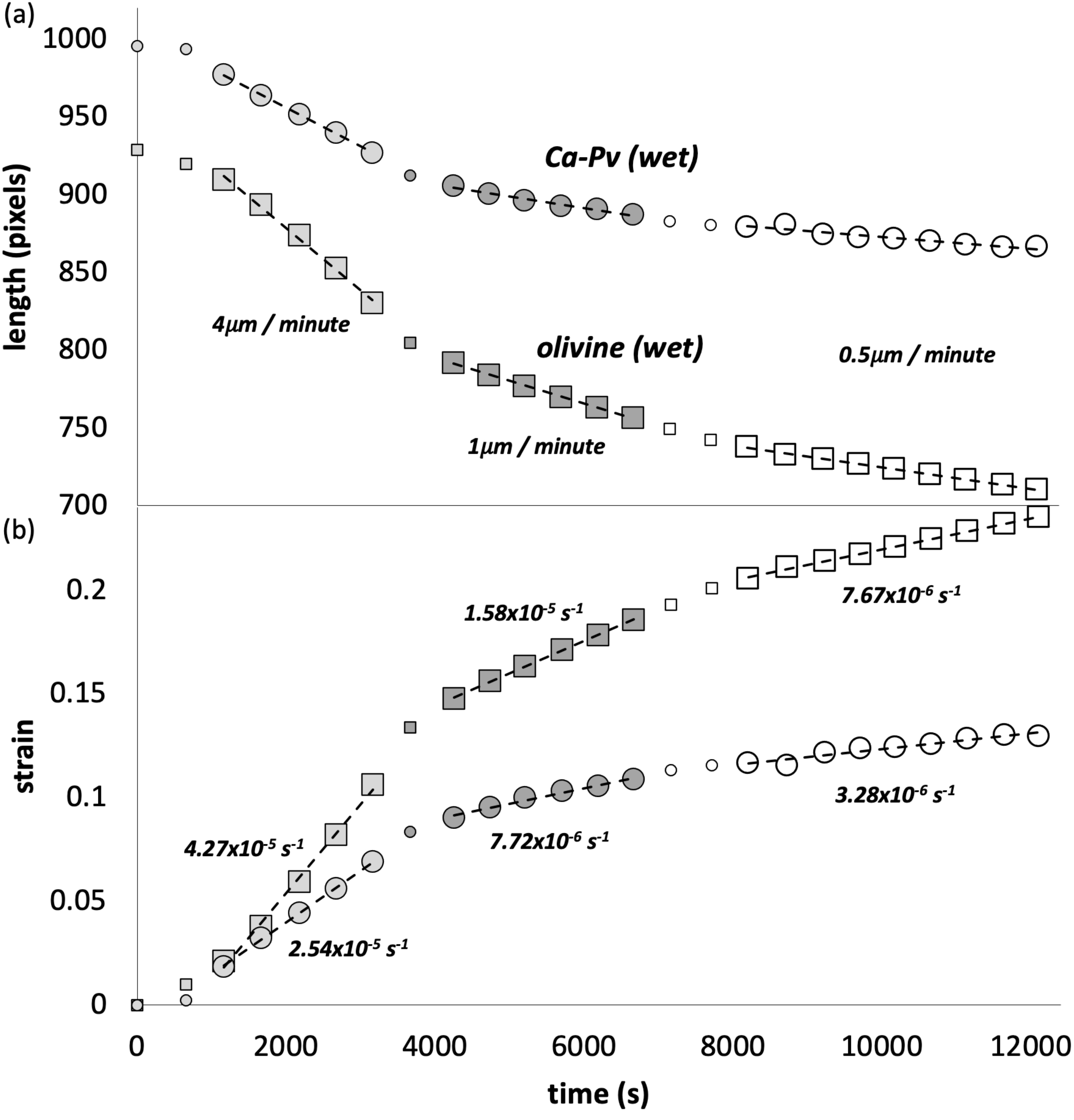
(a)
1000
950
900
850
800
750
700
length (pixels)
Ca-Pv (wet)
olivine (wet)
4μm / minute
1μm / minute
0.5μm / minute
(b)
0.2
0.15
0.1
0.05
0
strain
4.27x10-5 s-1
2.54x10-5 s-1
1.58x10-5 s-1
7.72x10-6 s-1
7.67x10-6 s-1
3.28x10-6 s-1
0
2000
4000
6000
8000
10000
12000
time (s)

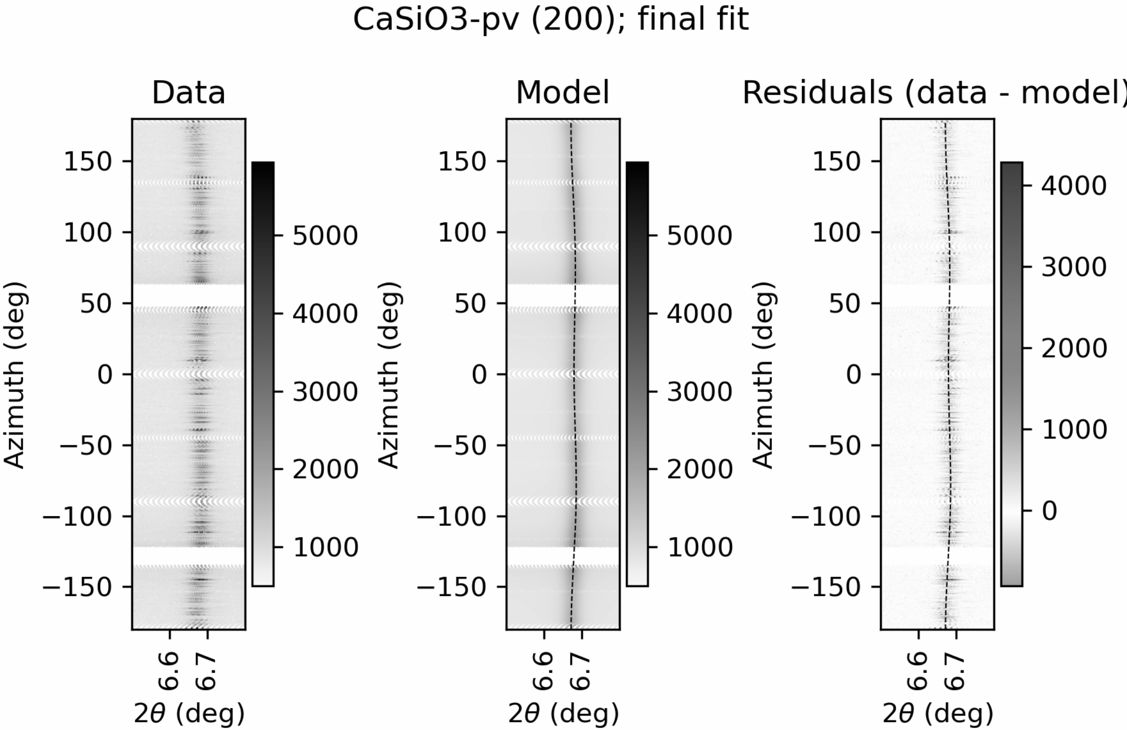
CaSiO3-pv (200); final fit
Data
Model
Residuals (data - model)
Azimuth (deg)
150
100
50
0
−50
−100
−150
2θ (deg)
6.6
6.7
5000
4000
3000
2000
1000
0

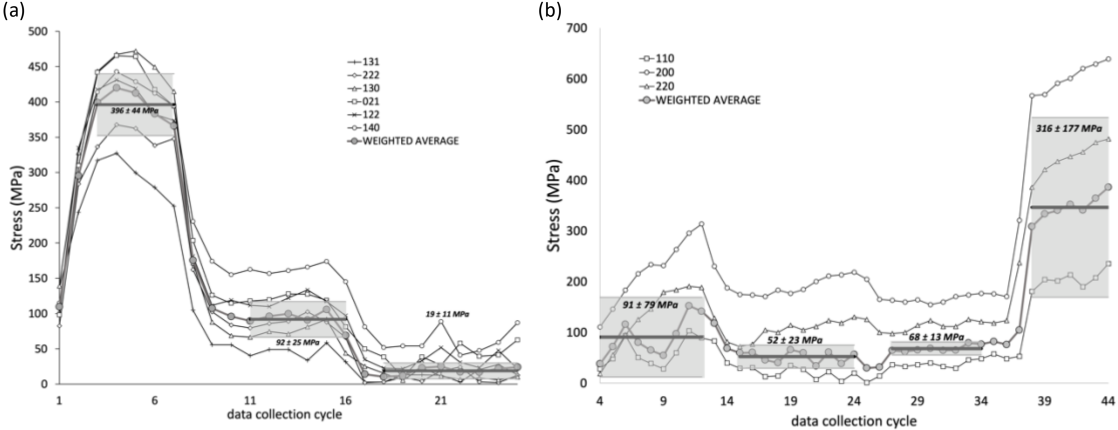
(a)
500
450
400
350
300
250
200
150
100
50
0
Stress (MPa)
1
6
11
16
21
data collection cycle
131
222
130
021
122
140
WEIGHTED AVERAGE
396 ± 44 MPa
92 ± 25 MPa
19 ± 11 MPa
(b)
700
600
500
400
300
200
100
0
Stress (MPa)
4
9
14
19
24
29
34
39
44
data collection cycle
110
200
220
WEIGHTED AVERAGE
91 ± 79 MPa
52 ± 23 MPa
68 ± 13 MPa
316 ± 177 MPa

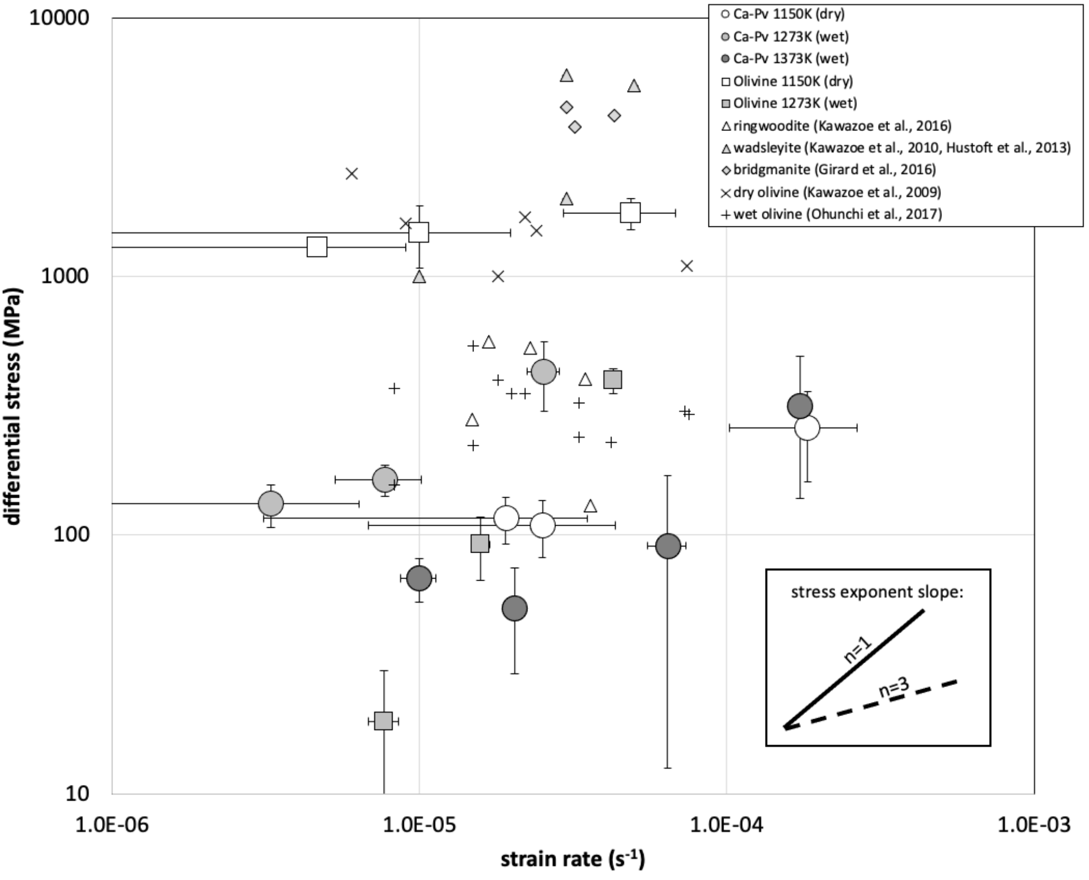
○ Ca-Pv 1150K (dry)
● Ca-Pv 1273K (wet)
● Ca-Pv 1373K (wet)
☐ Olivine 1150K (dry)
■ Olivine 1273K (wet)
△ ringwoodite (Kawazoe et al., 2016)
▲ wadsleyite (Kawazoe et al., 2010, Hustoft et al., 2013)
◆ bridgmanite (Girard et al., 2016)
× dry olivine (Kawazoe et al., 2009)
+ wet olivine (Ohunchi et al., 2017)
stress exponent slope:
n=1
n=3
10000
1000
100
10
1.0E-06
1.0E-05
1.0E-04
1.0E-03
differential stress (MPa)
strain rate (s^{-1})